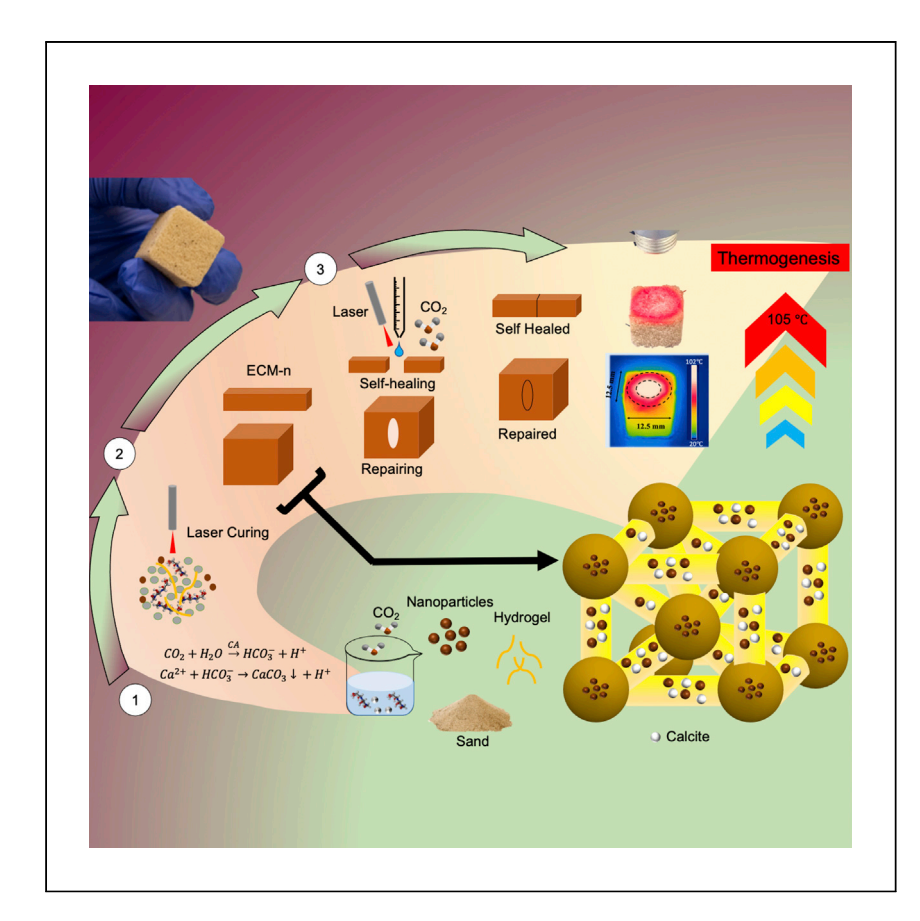


#### **Article**

# Curing and self-healing of enzymatic construction materials using nanoparticles



Wang et al. report the application of nanoparticle methodology where particles are added to enzymatic construction material (ECM) to allow curing at ambient temperatures without the need for heat/desiccation for on-site fabrication. In addition, the material can be rapidly repaired when built-in flaws are introduced.

Shuai Wang, Suzanne Scarlata, Nima Rahbar

nrahbar@wpi.edu

#### Highlights

Introduction of curing method that allows for on-site fabrication

Nanoparticles reduce the curing period in a recently developed ECM-n

Curing can be carried out using a low-power laser or other light sources

ECM-n can be used as a multifunctional thermal element

Wang et al., Cell Reports Physical Science 3, 101039

September 21, 2022 © 2022 The Author(s). https://doi.org/10.1016/j.xcrp.2022.101039





#### **Article**

## Curing and self-healing of enzymatic construction materials using nanoparticles

Shuai Wang, <sup>1</sup> Suzanne Scarlata, <sup>2</sup> and Nima Rahbar<sup>1,3,\*</sup>

#### **SUMMARY**

Preparation of construction materials on site may offer advantages in transportation and storage. However, a major limitation of on-site preparation of some materials is the need for heat and oven desiccation for adequate curing. Here, we describe a method that allows rapid curing under ambient conditions through the addition of 0.1% iron oxide nanoparticles to a carbon-negative enzymatic construction material (ECM) to make ECM-n. Specifically, we show that a low-power laser (3W at 808 nm) can cure ECM-n to an optimal mechanical strength in 12 h, which can be compared to the 14-day period needed for *in situ* air drying. In addition, the incorporation of nanoparticles allows rapid self-healing of large-scale flaws and that incandescent light can be used if lasers are not available. This method establishes an on-site manufacturing capability for ECM-n and other construction materials and supports thermal controllability of the local structure in low-temperature regions.

#### **INTRODUCTION**

Global carbon emissions have grown rapidly since the 21st century and have become one of the main contributors to the greenhouse effect, leading to the rapidly fluctuating weather patterns that accompany global warming. Concrete is the most used material on the planet, and its manufacturing accounts for 8% of human-made global carbon emissions. 1,2 It has been reported that each kilogram of concrete production releases 0.65-0.92 kg carbon dioxide based on a cement plant with modern technology and equipment.<sup>3,4</sup> For these reasons, we have recently developed a concrete substitute that sequesters rather than generates CO2. This sand-based material, coined enzymatic construction material (ECM) contains an enzyme called carbonic anhydrase (CA), which catalyzes carbonation and accelerates calcium carbonate precipitation in a process that consumes CO<sub>2</sub>. The enzyme generates large quantities of crystals that bridge with natural sand, resulting in a solid material with outstanding compressive strength<sup>5</sup>—three times higher than the minimum acceptable for cement mortar<sup>6</sup> and other biological building materials. 7,8 Also, the self-healing ability of ECM was shown in our studies where the material was fractured and healed six times. This ability to self-heal makes ECM practical and durable in environments where the material is subjected to freeze-thaw cycles.

Traditional concrete curing properly requires an adequate amount of moisture for continued hydration and 28 days to achieve mechanical strength. 9,10 Compared with concrete, ECM obtains maximum compressive strength in 24 h by oven heating or >1 week under natural desiccation. However, to reduce the time cost, the application of an oven certainly makes the on-site construction challenging. Here, we show that adding a trace amount of iron oxide nanoparticles to ECM generates an



<sup>&</sup>lt;sup>1</sup>Department of Civil and Environmental Engineering, Worcester Polytechnic Institute, Worcester, MA 01609, USA

<sup>&</sup>lt;sup>2</sup>Department of Chemistry and Biochemistry, Worcester Polytechnic Institute, Worcester, MA 01609, USA

<sup>&</sup>lt;sup>3</sup>Lead contact

<sup>\*</sup>Correspondence: nrahbar@wpi.edu https://doi.org/10.1016/j.xcrp.2022.101039



improved material called ECM-n that is easily cured with a low-power laser, or incandescent light (the curing incandescent light experiment set up can be found at support information, Figure S1). This method, based on studies of laser-induced nanoparticles application in hyperthermia therapy 11-14 uses the exothermic behavior of iron oxide nanoparticles under external electromagnetic (radiofrequency, microwave, and laser) excitation. Specifically, we show that the ECM-n samples cured for 12 h under a 3W laser (808 nm wavelength) have compressive strength similar to that of ECM. In addition, fabricating large flaws in ECM-n samples showed accelerated repair with laser exposure and the samples regained mechanical strength and properties comparable to original, flawless samples. Our method is supported by studies describing surface temperature profiles during curing and post-curing and the distribution of nanoparticles in ECM-n samples. Complimentary numerical analyses of heat transfer under laser support the experimental results, which reveal the underlying thermogenesis mechanism. While the studies focus on the sand-based ECM-n, our method can be generalized to other materials that would benefit from rapid on-site curing.

#### **RESULTS AND DISCUSSION**

#### Laser-induced curing of ECM-n

The composition of ECM (i.e., sand, gelatin, carbonic anhydrase) is extensively described in our previous publication.<sup>5</sup> To verify the effect of nanoparticles on ECM curing rate, the 12.5-mm cubic ECM-n (ECM with 0.1% iron oxide nanoparticles) and ECM were fabricated using the same method and subjected to the same power laser. Both specimens were cured under a 3W laser (808 nm wavelength) for 12 h to obtain a specific degree of dehydration through mass loss evaluation (Figure S2A). As shown in Figure S2B, the maximum surface temperature of ECM-n reaches 110°C in 12 h to obtain full dehydration, which shows a stable mass after 9 h. In contrast, the maximum surface temperature of ECM increases to only 62°C and maintains the mass loss condition. The surface temperature of ECM-n and ECM within the first curing hour was recorded in Figures 1A-1D. Figure 1A shows the early curing configuration of a cubic 12.5 mm ECM-n in a silicon mold where the sample was placed under a 3W continuous wave laser (808 nm) at a 2-cm distance for 60 min, while the surface temperatures at the top and side were recorded by a thermal camera for 70 min. We find that the maximum surface temperature of the ECM-n sample increases from  $26^{\circ}$ C to  $81.5^{\circ}$ C (sample: n = 5, median: med = 81.5, SD = 3) (Figures 1B and 1C). In contrast, the temperature of all ECM samples without nanoparticles never rises above 60°C (n = 5, med = 53, SD = 5.7). The temperature distribution is non-uniform, with the maximum temperatures occurring within the center of the laser beam. From the temperature curves in Figure 1D, the heating rate of ECM-n is ~2-fold higher in the first 20 min, the cooling rates of both were similar, reaching room temperature in 5 and 2 min, respectively, and giving a cooling rate of  $11^{\circ}$  C/min (n = 5, SD = 0.82) for ECM-n and  $15^{\circ}$  C/min for ECM (n = 5, SD = 1.63). These data indicate that the addition of nanoparticles does not significantly increase the specific heat capacity of ECM. Due to the low specific heat of nanoparticles, the nanoparticles accelerated curing by photothermal effect.

#### Heat release analysis during the initial curing

To quantify the early curing kinetics of ECM-n, we used isothermal calorimetry (ITC) to understand the relationship between time and heat flow of ECM-n. In Figure 2, we compare heat flow in ECM-n samples at 25°C and 60°C. One heat flow peak was detected at two different temperatures in 30 min and both peaks appeared immediately after injecting the enzyme calcite solution; the peak at 60°C is more distinct than the peak at 25°C. The intensity of the peak increased with the temperature,



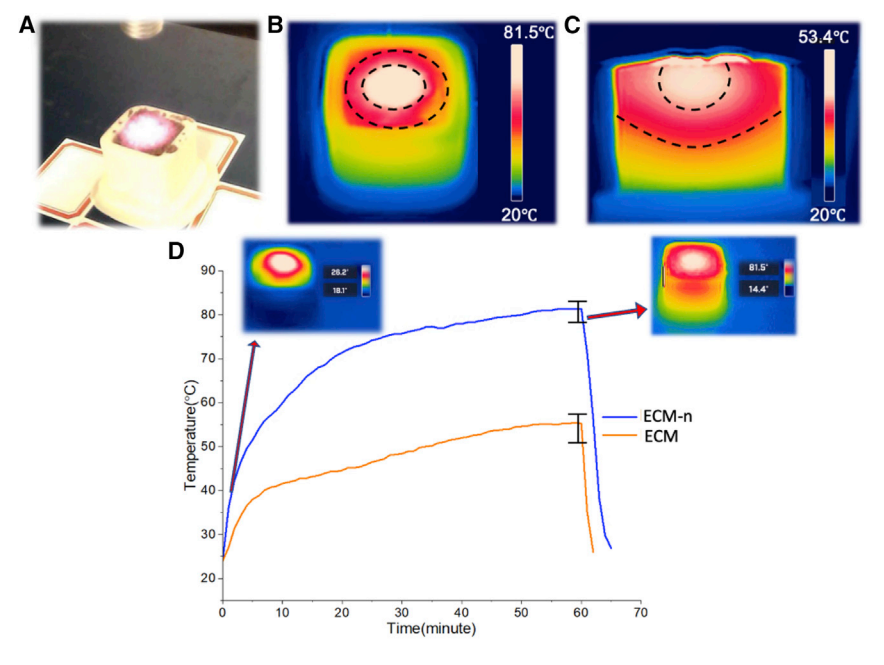


Figure 1. The laser induces ECM-n curing

- (A) The picture of the experimental setup.
- (B) Top view of the temperature variation of ECM-n. The maximum temperature rises to  $81.5^{\circ}$ C at 60 min (n = 5, med = 81.5, SD = 3).
- (C) The side view of the temperature contours in ECM-n.
- (D) The temperature as a function of curing time at the center of a 0.1% nanoparticle-modified ECM-n 12.5 mm cubic sample surface under 3W laser induction compared with ECM without nanoparticles. The data of ECM and ECM-n were taken from a median group of 5 independent samples (n = 5).

indicating that the elevated temperature significantly enhances the degree of dissolution. The higher dissolution of the raw materials at higher temperatures provides more scaffoldings for the following bridging steps, and thus accelerated the early strength development and the final setting of the ECM-n samples.

#### Laser heating ECM-n in low and room temperatures

The application of laser heating was also explored on cured ECM-n. Figures 3A–3C demonstrate the photothermal effect on cured ECM-n at ambient temperature induced by a 3W continuous wave laser. Figure 3A shows the experimental setup. Figures 3B and 3C show the top and side views of the contours of temperature for an ECM-n sample subjected to laser heating for about 1 h, respectively. For a sample distance of 2 cm from the laser, the peak temperature is concentrated in the center of the sample surface and spreads radially outward into the surrounding surface region. The results indicated that the maximum temperature of the ECM-n surface increases to 102°C at room temperature. The influence of heat convection on the side can be observed in Figure 3C. The temperature profile shows a curve in the form of layers, with the lowest temperature at the furthest position from the heat source.

The photothermal effect of cured ECM-n was also explored at low temperatures. The time sequence of the experiment is presented in Figure 3D. The sample was stored in a  $-20^{\circ}$ C freezer to obtain a homogeneous temperature on the surface. The schematic on the left shows the experimental setup. The sample was then illuminated in a freezer by the 3W laser. A thermal camera was exploited to record the temperature of the sample surface under illumination for 10 min. At the center of the top face of



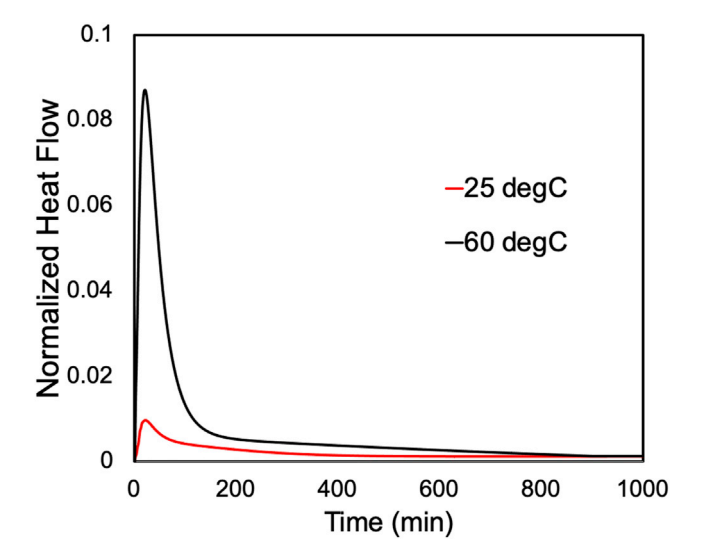


Figure 2. The normalized heat flow for the initial curing of ECM-n at 25°C and 60°C
The behavior of the ECM-n heat flow after injecting an enzyme-calcite solution under 2 different temperatures. Both peaks can be identified within 6 min and then tend to plateau.

the sample, the temperature increased from  $-20^{\circ}\text{C}$  to a maximum of  $60^{\circ}\text{C}$  in 10 min. The above findings provide a new path for ECM to be used as a thermally controllable construction material.

#### Thermal modeling of laser heating

To further demonstrate the thermogenesis ability of the ECM-n, the computational laser heating was modeled using the finite element method (FEM) and the software package COMSOL Multiphysics 6.5 (COMSOL, Burlington, MA). The details of the thermomechanical modeling can be found in the supplemental experimental procedures, Table S1, and Figure S3. Figure 4 presents the maximum temperature as a function of time for an ECM-n sample at three different laser powers. It can be observed that the simulation results are slightly less than the corresponding experimental results, and the normalized temperature profiles are proportional to the laser power.

In the process of heating the ECM-n by laser, heat transfer will happen through three main mechanisms: conduction, convection, and radiation. The static laser beam follows Fourier heat conduction law. <sup>15</sup> The heat distribution within the ECM-n is then determined by the following transient heat transfer equation:

$$\rho C_p \frac{\partial T}{\partial t} = \nabla \cdot (k \nabla T) + \alpha Q$$
 (Equation 1)

where  $\rho$  is the density equal to 1,660 kg/m³,  $^5$   $C_p$  is the heat capacity of sand equal to 840 J/kg • k, T is the temperature, t is the time, and the thermal conductivity of iron oxide is denoted as k, which is equal to 2.7 W/m • k.  $^{16}$  A thermal conductivity parameter was used to represent the iron oxide in this ECM-n model. This is done for two reasons: (1) During the dehydration process, the gelatin undergoes a phase change from a gel to a crystalline state, which complicates the modeling process, and (2) the iron oxide possesses a higher thermal conductivity than sand and gelatin, which significantly affect the temperature of the system. The absorption coefficient,  $\alpha$ , depends on the object material and the interaction between the object material and the wavelength (808) of the laser, where most models use a constant absorption coefficient by neglecting the influence of incident angle and temperature.  $^{17}$  To



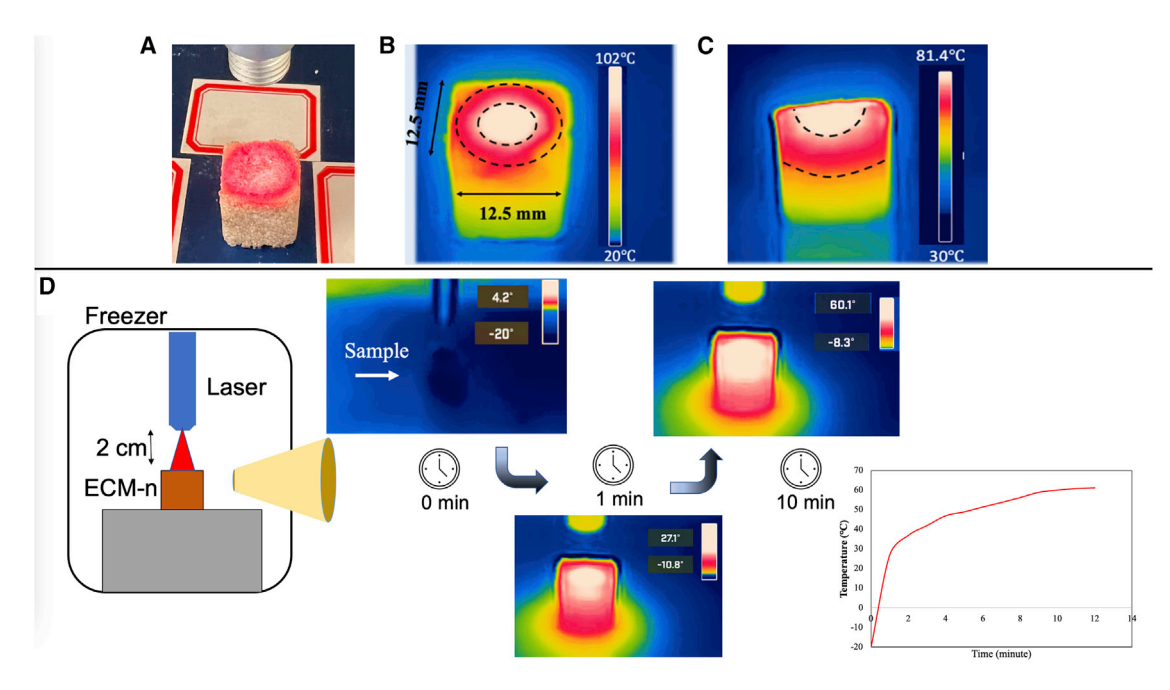


Figure 3. The infrared thermal images of cured ECM-n thermal effect at different temperatures

- (A) The laser heating experiment was set up at ambient temperature for ECM-n.
- (B) The spatial view of the ECM-n at 1-h laser irradiation.
- (C) The side view of the sample at 1 h of laser irradiation.
- (D) The process of laser heating of ECM-n at  $-20^{\circ}$ C freezer and the top surface temperature of the sample was raised to  $60^{\circ}$ C in 10 min.

simplify, the absorption coefficient was assumed to be 1 in this study, and Q (W/ $m^3$ ) is the laser heat source term. The boundary conditions for Equation 1 at the side of ECM-n are heat transfer by convection, and at the top surface is radiation. The convection (Newton's law of cooling) in the laser heating process is expressed by

$$q_{con} = h(T_{ext} - T) = -\hat{n} \cdot - (k\nabla T)$$
 (Equation 2)

The radiant heat flow rate of the object can be computed based on the empirical formula of Boltzmann's law by

$$q_{rad} = \varepsilon \sigma (T_{amb}^4 - T^4)$$
 (Equation 3)

Heat convection always is transferred by gas or liquid media. In this study, the air is the major media in the convection. For simplicity, the heat convection coefficient is considered to be uniformly distributed and equal for all surfaces of the boundary, where h, the natural air heat convection coefficient, is  $25\,\mathrm{W/m^2} \cdot k$ .  $^{18}\,\varepsilon$ , the emissivity of sand is estimated to be  $0.95.^{19}\,\sigma$  is the Stefan-Boltzmann constant, and  $\hat{n}$  is the direction vector.  $T_{\mathrm{ext}}$  and  $T_{\mathrm{amb}}$  are the medium air and room temperatures, respectively, where both are assumed to be 300 K.

For a continuous wave laser mode, the fundamental mode of the Gaussian beam is generally preferred, <sup>20,21</sup> and the Gaussian heat source is provided accordingly. The rate of heat generation by the Gaussian profile of a transverse model optical intensity of order n can be given by

$$Q(x, y) = pf * f(x, y)$$
 (Equation 4)

Here, the laser power intensity  $(W/m^2)$  can be expressed by

$$pf = \frac{P}{\pi * r^2}$$
 (Equation 5)



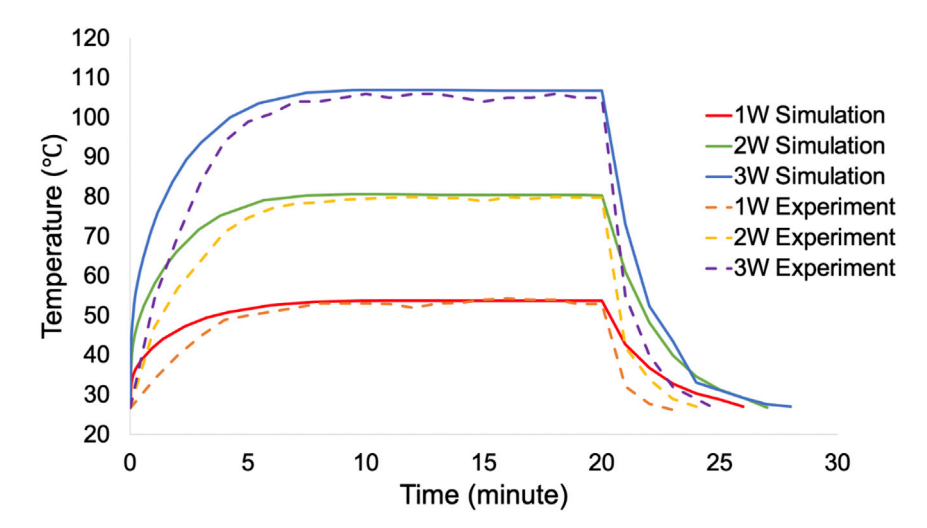


**Figure 4.** The comparison of experiment and simulation in laser heating ECM-n
Temperature changes along the time and laser power for the ECM-n in 30 min. The laser was removed for 20 min and the materials started to cool to the ambient temperature. The results from experiments and the predictions show reasonable agreement.

and the Gaussian laser term is

$$f(x,y) = \exp\left[-2\left(\frac{x^2+y^2}{r^2}\right)^n\right]$$
 (Equation 6)

where the laser beam was defocused to a processing radius of 6 mm. The Gaussian laser intensity profile of order 1 was implemented in Figure S3B. The reliability of the simulation was assessed in comparison with the experimental data, according to the heat transfer theory, and the temperature stabilized to a relatively steady state at 10 min under continuous heat energy input, which is in agreement with the experimental results at different laser power. Both temperature profiles of the experiment and simulation are raised to ?51, 78, and  $105^{\circ}$ C at 1-, 2-, and 3W laser, respectively.

#### Self-healing assessment under laser curing

The self-healing ability of ECM had been extensively assessed in our previous publications. This potential feature was also demonstrated with a similar set of experiments with nanoparticle-modified ECM (ECM-n), which is shown in Figure 5. We find that the ECM-n cuboid sample autonomously self-healed with laser heating without an external force or additional treatment. When fractures occur, the scaffold bridges are exposed on the fracture faces, which implies that the mineral bridges are the weak link in the microstructure of ECM.

The fractured sample was assembled in a silicon mold, and then the  $CO_2$  gas was sprayed continuously on the fracture region. In the healing process, the precipitated  $CaCO_3$  crystals were expected to gradually grow on the scaffold and eventually bridge the fracture interface during laser heating. It was noted that the additional carbonic anhydrase was added with the calcium solution in the crack area; this is due to the decreasing enzyme activity during laser photo illumination. The fracture cuboid ECM-n sample was treated with calcium solution with a trace amount of enzyme (5  $\mu$ L, 2.9 mg/mL) compared with the sample without enzyme treatment in the calcium source agent, which presented more crystals on the repaired crack after laser curing (Figure S4). The macroscale characterizations of the self-healing process can also be observed from the temperature profile of the sample. The temperature profile contour changes during the healing process, as



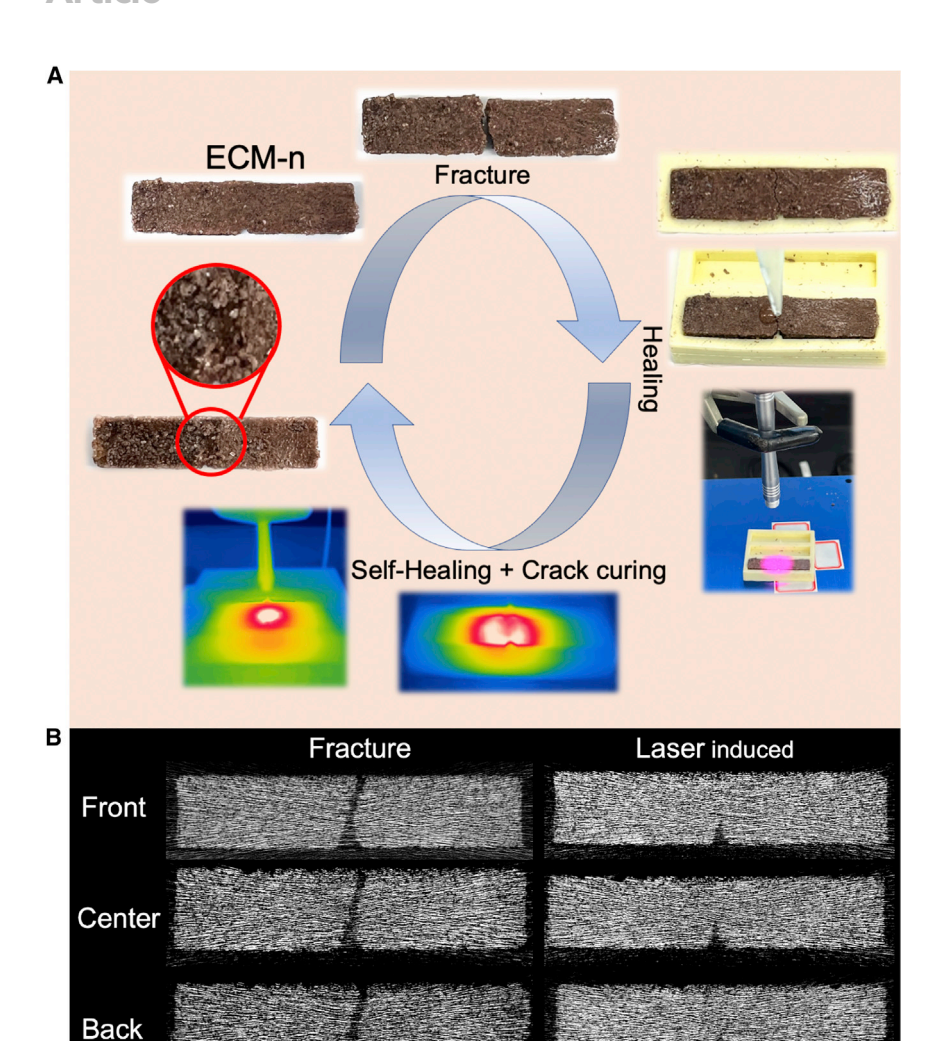


Figure 5. The schematic illustration of the self-healing capability of ECM-n beam via laser-induced heating

(A) A trace amount of calcium-enzyme solution was added to the fractured area. Then, ultra-pure  $CO_2$  was aerated on the surface for 15 min. The 3W laser was conducted in the same location over 4 h. The heterogeneous shape of the high-temperature region (white color) develops into a circle gradually. (B)  $\mu$ -CT scanned images of fracture and laser healing ECM-n beam at the front, center, and back layers.

expected because the nanoparticles are carried by a fluid medium and diffused until the sample is desiccated. The 4.1  $\times$  3.5 mm fracture surfaces were fully repaired after 4 h of laser treatment. The resulting ECM-n has the same self-healing capability as ECM and provides a potential application for outstanding material durability. We also used microcomputed tomography ( $\mu$ -CT) scanning to characterize and diagnose the internal and external microstructures of cracks within the ECM-n matrix (Figure 5B). The  $\mu$ -CT scanning images clearly show the crack path disappearing in three display layers (front, center, and back), indicating that the internal crack has self-healed as predicted by laser photo illumination.

#### ECM-n morphology and crystallinity characterizations

The optical and scanning electron microscopy (SEM) images of the morphology of ECM and ECM-n in multiscale were presented in Figures 6A-6I, showing a variation

1<sub>mm</sub>



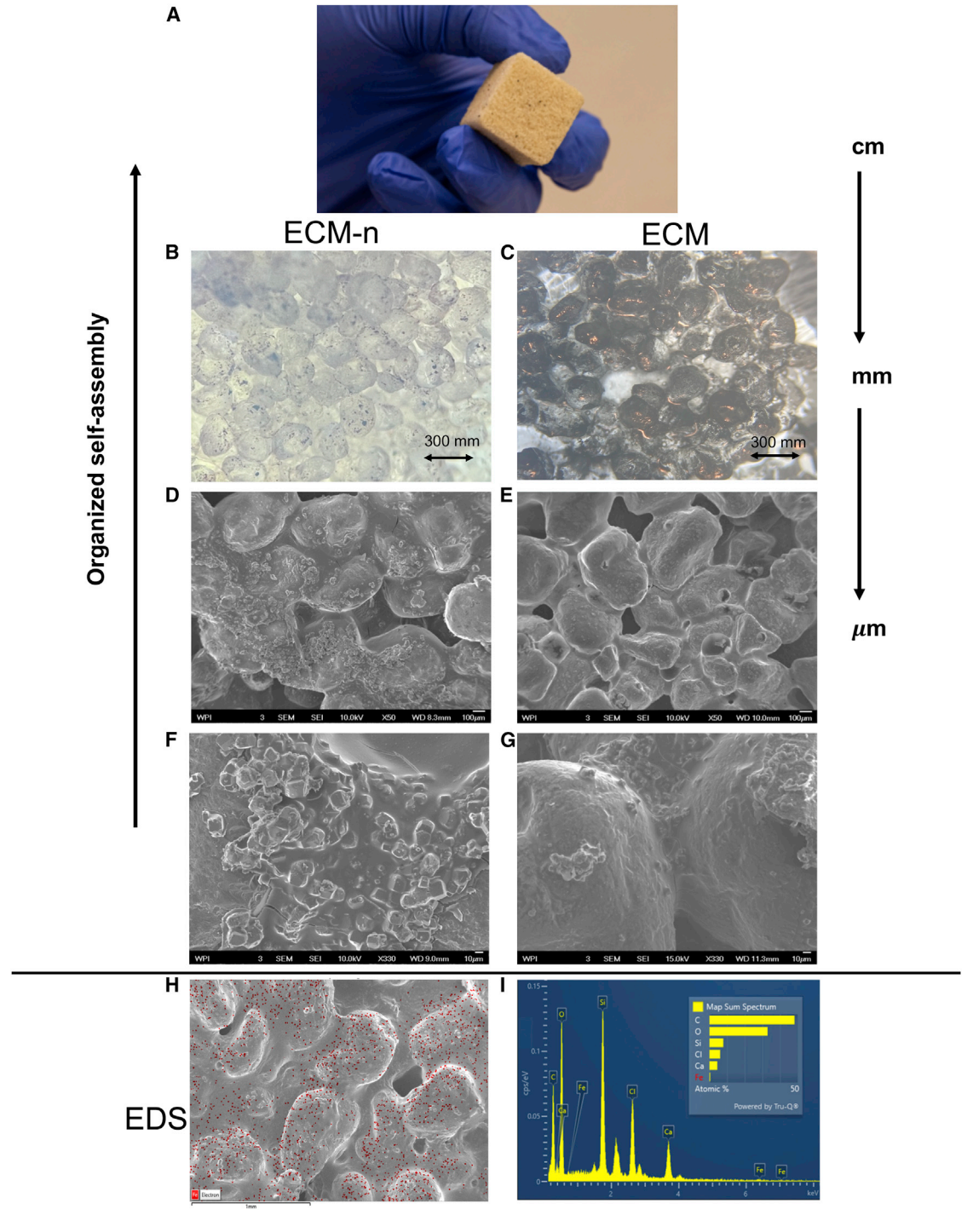


Figure 6. Comparing the multiscale microstructure and mineralization of ECM-n (left) and ECM (right)

(A) The real size of ECM-n in the hand.

(B–E) SEM and optical images of laser-cured ECM-n and oven-cured ECM showing that the scaffold bridges and calcite crystals are distributed uniformly.

(F and G) Higher magnification SEM images of scaffold bridges formed by laser curing (F) and oven curing (G).

(H and I) (H) EDS mapping images of the nanoparticle distribution in the matrix and (I) the major chemical compositions.

#### **Article**



in calcite crystals size at  $?10~\mu m$ . Detailed morphological characterization indicates that the laser-treated surfaces and the structure of ECM-n are similar to ECM without nanoparticles and cured in an oven. Calcite crystal distribution and the dimension of the hydrogel scaffold were not affected by the laser curing. The ordered structures were well assembled in ECM-n and ECM to efficiently shield the crack propagation. Although the sand particles and calcite crystals were assembled randomly within the polymeric scaffold, the overall view is similar to a body-centered cubic (BCC) crystal. In the plane view, the sand particles in both samples are connected with bridges in at least four directions. Due to the characterization of BCC structural type, sand slurry materials show a high ductility during the bending test, and with a high strain at 0.0032 compared with a normal weight concrete in the range from 0.002 to 0.003. As a result, the local application of the photothermal effect by iron oxide nanoparticles exhibits a mild effect in ECM-n, showing the high extent of stability and mechanical strength in sand slurry materials structure.

The nanoparticle distribution in ECM-n was also investigated by energy dispersion spectroscopy (EDS), optical microscopy, and Raman spectroscopy, as shown in Figures 6B, 6H, and S5, respectively. The EDS and optical images clearly show the nanoparticles distributed on each of the sand particles, correlating to a spherical temperature profile. The slight aggregation of nanoparticles occurring on the surface is due to the lack of surfactants during nanoparticle preparation. The surfactant coating consists of a variety of ester-based materials that depend on environmental factors at varying levels of chemical complexity; thus, only physical treatment was applied to the nanoparticles by the ultrasonic method to avoid a negative impact on the medium.

To further identify the distribution of nanoparticles as well as the precipitated crystals, four different locations on the sample surface were spotted by Raman spectroscopy. Raman spectroscopy is a nondestructive analytical technique based on changes in the scattering of low-energy light off material and can be used directly on the whole sample. Figure S5 displays the locations on the ECM-n surface that correspond to calcite and gamma  $Fe_2O_3$ . The spectra were processed and plotted proportionally by fitting the Gaussian function. The Raman characteristic peak of calcium carbonate is relatively narrow, indicating a high extent of crystallization, and the intensity of the peak is higher, indicating a higher content of calcite crystals and iron oxide nanoparticles in this region of the sample surface. The above results show that the nanoparticle distribution in the ECM-n achieves the desired effect.

We sought to understand whether the crystallinity and morphology of crystals generated by enzyme catalysis were influenced by laser illumination. Our previous study has proven that the enzyme product is calcite through Fourier transform infrared spectroscopy (FTIR) and powder X-ray diffraction (pXRD). The typical pXRD patterns in Figure S6 show the presence of precipitated calcium carbonate on ECM-n after laser curing, where a diffraction peak is observed at  $2\theta = 29.6^{\circ}$ , which agrees with the reference spectrum for calcite. The result verifies the crystallinity of the enzyme product as calcite. The morphology is supported by the SEM images in Figure 6.

#### Mechanical properties of repaired ECM-n

Designing high-performance construction building materials with excellent compressive strength is a long-standing engineering problem. Our previous studies had investigated the self-healing ability and tensile strength of ECM by oven desiccation, while the compressive strength after repairing still needs to be verified. Here,



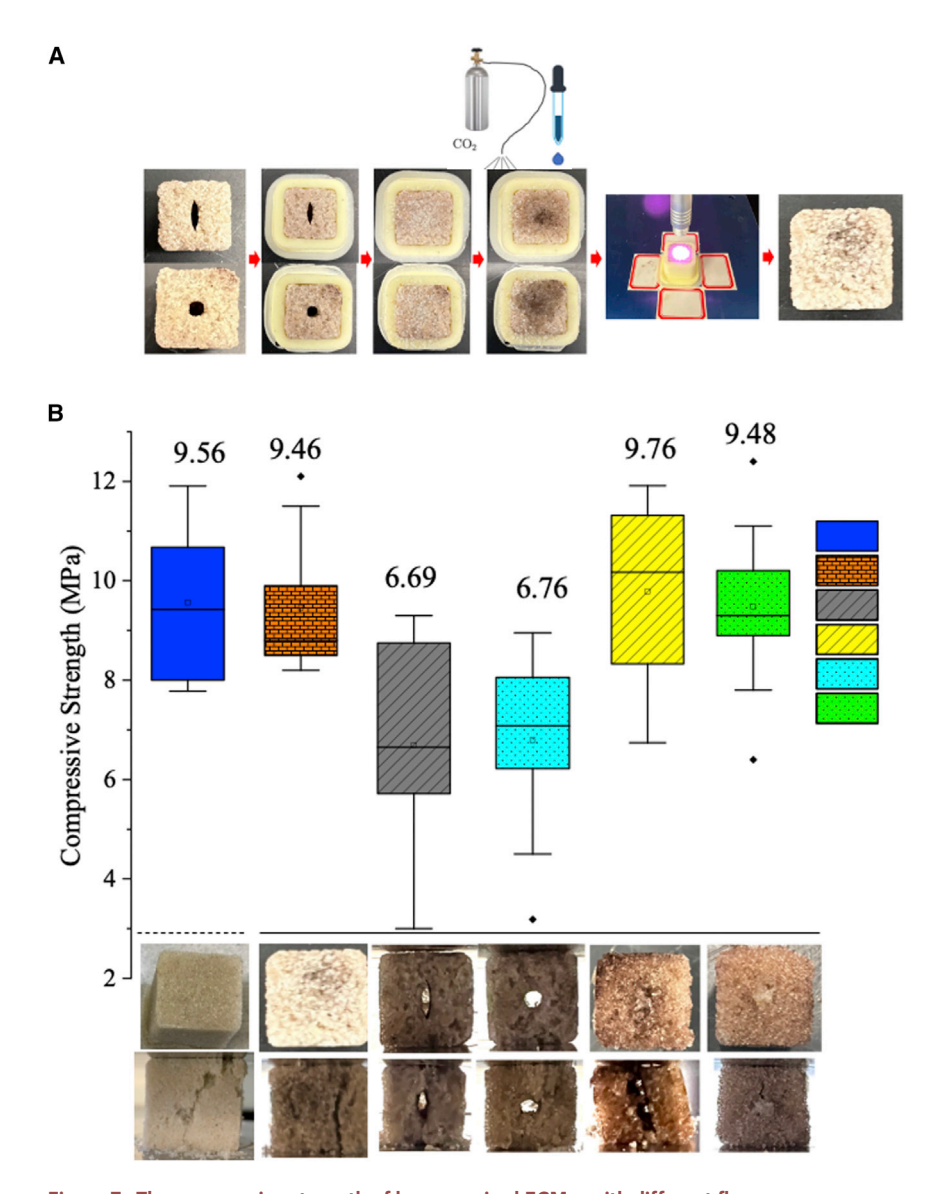


Figure 7. The compressive strength of laser-repaired ECM-n with different flaws

ECM-n samples with different flaw shapes were repaired and compared with oven-cured ECM. (A and B) (A) The laser repairing paradigm of ECM-n: the mean results are shown above each dataset, and a typical sample is shown at the bottom in (B). The compressive strength of ECM, in order from left to right are oven-cured ECM (n = 12, blue, med = 9.56, SD = 1.49), laser-cured ECM-n (n = 10, brown, med = 9.45, SD = 1.44), elliptical flaw ECM-n (n = 10, gray, med = 6.69, SD = 1.92, p = 0.003), circular flaw ECM-n (n = 10, yellow, med = 6.76, SD = 1.79, p = 0.004), repaired elliptical flaw ECM-n (n = 10, light blue, med = 9.76, SD = 1.86, p = 0.43), and repaired circular flaw ECM-n (n = 10, green, med = 9.47, SD = 1.75, p = 0.48).

we investigate the repair of large-scale notches while applying laser. To study the repair performance of the proposed mechanism on laser-induced curing of ECM and ECM-n, cubic-shaped specimens were fabricated for compressive testing, with two types of circular and elliptical flaws. The control and flawed samples are shown in Figure 7. It is noted that the ECM-n samples were cured by laser and the flawless ECM samples were cured in the oven. The laser-induced repairing experiment is shown in Figure 7A. The normalized values of compressive strengths compared to the control are presented in Figure 7B. The ECM-n samples, with a

#### Article



vertically oriented elliptical flaw that is 6 mm tall and 1.5 mm wide and extends through the cubic sample through the entire 12.5-mm depth, represent a macroscale crack that exhibits 74% of the strength of the undamaged control specimens. The samples with a circular flaw of 2 mm diameter and extending through the entire depth of the cube sample of 12.5 mm show ?70% of the strength of the undamaged control specimens.

The compressive strength results show that cube-shaped samples with built-in flaws can regain their original compressive strength by adding the calcium enzyme mixed solution to the original sand gelatin matrix. The material was then bubbled with ultrapure carbon dioxide for 10 min. This is followed by the application of the laser for curing for 12 h. The samples with the largest size of the repaired flaws (6 mm in vertical direction) still exhibit the capability of the proposed method in the repair of the ECM-n specimens. It must be noted that both repaired flaw shape samples slightly outperform the control samples with respect to the average compressive strength. The compatibility of the existing matrix with the additional sand-gelatin repair agent is excellent, and the repair process also allows additional curing of the original matrix, leading to an overall stiffer structure.

Comparing the results, the variation in the strength of the elliptical flaw and repaired elliptical flaw ECM-n samples is relatively high. This difference is mainly due to the geometric offset of the elliptical flaw during the sample preparation in the silicone mold. It is noted that the samples with prefabricated elliptical and circular flaw fail by crack initiation at the flaw and growth resulting from dilatation due to Poisson's effect. The p value of flawed ECM-n samples is <0.05, which leads to significant changes in the performance of the structure, while the p value of repaired elliptical and circular flaw ECM-n are within statistical error (>0.05). Therefore, ECM-n with flaws maintains mechanical stability after repair by the laser.

#### Embodied energy and CO<sub>2</sub> of ECM/ECM-n

To visualize the impact of ECM/ECM-n on sustainable environmental protection and various types of construction materials, we compare the embodied energy versus the embodied  $CO_2$  and specific strength versus the embodied  $CO_2$  associated with different construction materials (Figures 8A, and 8B). Except for ECM/ECM-n, embodied energy, embodied  $CO_2$ , and specific strength data were selected from the inventory published by Hammond and Jones and Ashby. <sup>22,23</sup> The Ashby diagram of embodied energy versus embodied strength shows that ECM/ECM-n consumes  $CO_2$  as seen by negative values compared to other construction materials. This is because the formation of the ECM/ECM-n requires the consumption of carbon dioxide. Furthermore, the ECM/ECM-n presents relatively low energy consumption.

The boundaries that were considered in this study are cradle to gate. Thus, the transportation consuming energy and manufacturing processes of ECM/ECM-n were recognized similarly to concrete in this report. The negative  $CO_2$  emissions and low-energy embodiment of ECM/ECM-n are because most of the components can be obtained directly in nature or by simple secondary processing. The enzyme, carbonic anhydrase, which is added in trace amounts, is isolated from bovine erythrocytes or other natural sources, which does not generate carbon dioxide, and requires little energy. The calcium can be obtained from natural brines as a by-product of synthetic soda ash production. Another low-carbon method is to produce calcium from hydrochloric acid and limestone. The process will generate hydrogen that can be directly burned or generated by fuel cells to obtain water, which can be achieved by true zero carbon emissions without polluting the environment. The gelatin is extracted by hydrolysis of biological material in a process



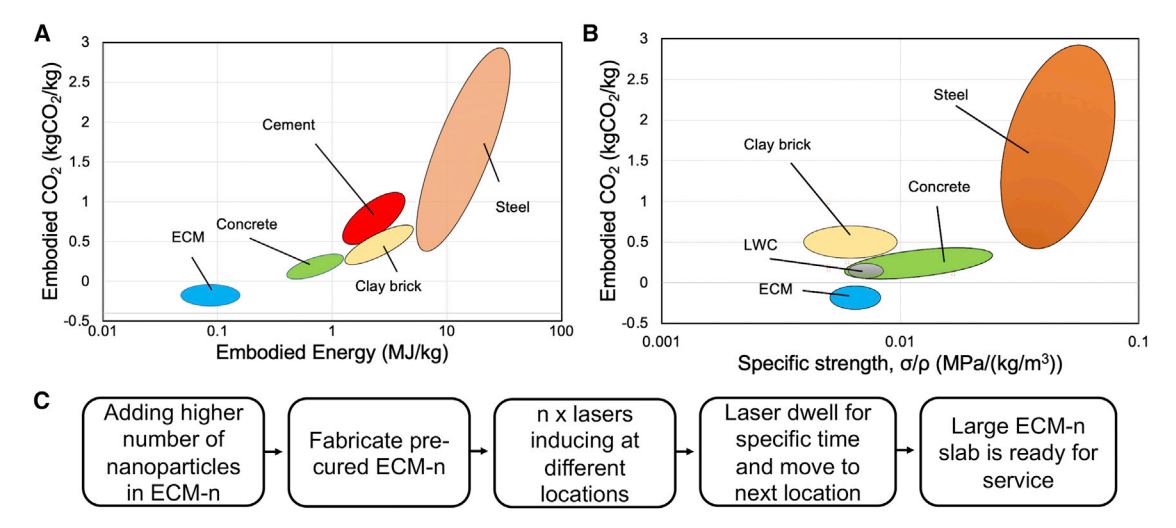


Figure 8. Ashby diagram and scaling up ECM-n procedures

Carbon footprint and mechanical properties of ECM/ECM-n compared to different construction materials.

(A) Ashby diagram of embodied  $CO_2$  versus embodied energy data for reference materials was extracted from the inventory published by Hammond and Jones.  $^{22}$ 

(B) Ashby diagram of specific strength versus embodied CO<sub>2</sub> for comparison with related construction materials.

(C) The basic procedures of fabricating ECM-n on construction site.

that is essentially zero emissions.  $^{26}$  In our paradigm, only 0.1% (by sand weight) nanoparticles were applied in the medium, and many researchers have proven that the nanoparticles are a clean product that can capture and use  $CO_2$  from the air.  $^{27-29}$  The specific mechanical properties of ECM/ECM-n were also compared with other construction materials in Figure 8B. Cracking is assumed to be the initiation of concrete failure. The specific strength of ECM/ECM-n was comparable to the lightweight concrete (LWC) and the minimum of the commercial concrete. There is no negative impact of nanoparticles between ECM and ECM-n, which result in the same mechanical properties as discussed in the section "Mechanical Properties of Repaired ECM-n."

Scaling up the concept of ECM-n from the lab to the construction site can be achieved in a few years. These materials can entirely replace LWC and masonry blocks in all of their applications. In particular, the ECM-n can rapidly be constructed for the temporary base, secondary structure, and pipe in extreme weather. Here, a guiding flowchart is provided as a reference (Figure 8B). From the above results, the effective area of ECM-n is proportional to the number of nanoparticles and the power of the laser. Therefore, in on-site construction, a higher number of nanoparticles and higher-power laser are suggested to apply on the ECM-n to guarantee the desired effects. For example, to fabricate a 10 x 10-ft ECM-n slab, pre-cured ECM-n can be prepared on the foundation, and then 10 industrial laser machines can be induced at different spots (we assume the effective area is  $0.5 \times 0.5$  ft). A trial experiment can be carried out in the field to develop a relationship between required depth and laser-inducing time. Designing the laser dwell at each spot for a specific time to achieve full curing (3W laser induces 4 h for a 12.5-mm depth) before moving to the next spot. The total time should be ?160 h without considering the ambient humidity and natural drying rate, but this will decrease exponentially with an increase in the number of nanoparticles added. However, achieving the balance between time effectiveness and power cost is the key to this process. Upon ECM-n slab completion, the potential for heat transfer applications (especially in winter) is unlimited.

#### **Article**



In this study, we established a curing protocol with the use of a trace amount (0.1% by mass) of nanoparticles and a low-power laser that we applied to the recently created ECM. The presence of nanoparticles and laser-induced curing preserved the integrity of ECM, including compressive strength and self-healing capability. A multiphysics model is provided for the future optimization of new functionalities of ECM production as emerging green technology applications, ranging from radiant heating to carbon sequestration techniques. Given the global environmental impact of the production of cement-based materials, the development and implementation of such novel functionalities are expected to foster the sustainable development of both the construction sector and our built infrastructure at large. This method may provide a step toward thermally controllable self-healing construction material.

#### **EXPERIMENTAL PROCEDURES**

#### Resource availability

#### Lead contact

Further information and requests for resources should be directed to and will be fulfilled by the lead contact, Nima Rahbar (nrahbar@wpi.edu).

#### Materials availability

This study did not generate new, unique reagents.

#### Data and code availability

All data generated and analyzed during this study are included in this article and the supplemental information.

#### Materials and methods

The ECM-n was fabricated in the top-to-down approach, as was the ECM for the entire study. The iron oxide nanoparticles (Fe<sub>2</sub>O<sub>3</sub>, gamma, high purity,  $\geq$ 99.5%, 20 nm) were purchased from US Research Nanomaterials (Houston, TX, USA). It was selected because of (1) its ultra-high thermal conductivity and (2) the size of the nanoparticles could easily fit in the void within the ECM structure. The Photon 3W Dental Diode Laser (Zolar Technology and Manufacturing, Mississauga, ON, Canada) was chosen in this study, which emits an infrared laser light beam ( $\lambda$  = 808 nm). The FLIR One iOS Pro-Grade Thermal Camera was used to measure the temperature of the heated surfaces of the samples.

#### Solution preparation

CA at 10  $\mu$ L at a 100- $\mu$ M concentration was stored in  $-20^{\circ}$ C until use in the experiment. A 0.1-M Tris solution was added to 200 mL of deionized (DI) water, and 10  $\mu$ L of CA was added to the beaker to create the enzyme buffer solution. A 2-M CaCl<sub>2</sub> solution in 200 mL of DI water were well mixed on the stirred plate for 2 min and cooled down to 30°C because of the exothermic reaction between calcium chloride and water. The enzyme buffer and CaCl<sub>2</sub> solution were combined in an Erlenmeyer flask to mix for additional 2 min. CO<sub>2</sub> gas was aerated into the flask at the rate of five bubbles per second. The foggy solution can be observed within 5 min, when the calcite crystals were catalyzed and formed small particles in the solution. The experiment ended by stopping the flow of CO<sub>2</sub> gas at the 15th minute.

#### **ECM-n** fabrication

For the preparation of ECM-n, a 10% (g/mL) gelatin by solution matrix was mixed thoroughly with number 50 (the sand retained on a 300- $\mu$ m sieve) white sand and filled the 12.5-mm 3-dimensional (3D) printed silicon cubic mold. Iron oxide nanoparticles (0.1% by sand weight) were added to the enzyme-calcite solution



(0.27 mL/g, solution volume/sand weight) by using an ultrasonic bath for 1 min and then quickly mixing for 30 s manually. The ultrasonication ensured that the nanoparticles were distributed homogenously in the mineral solution. Afterward, the solution was poured over the sand slurry matrix and vibrated for 2 min before laser curing. This procedure was used for obtaining a further distribution of nanoparticles in the sand slurry system, where the viscosity of the hydrogel avoids the agglomeration of nanoparticles.

#### Laser-induced curing of ECM-n

The laser diode corresponds to a heating power of 3W. The laser beam was transmitted through a fiberoptic cable to the tip of a cylindrical probe before propagating into the sample. The distance between the tip of the probe and the sample surface was set at 2 cm to achieve a laser spot size of 1 cm on the samples. The temperatures of the heated surfaces of samples were recorded with an infrared camera (FLIR One Pro). Subsequently, the 12.5-mm cubic sample was heated and dehydrated in the silicon mold for 12 h. The cuboid samples (38 mm in length, 8.3 mm in depth, 4.1 mm in width, and 1.1 mm in notch length) were fabricated in the same method. Due to the limited size of the laser beam, the cuboid sample was spotted at three different locations (left, center, and right) for 5 h at each point to achieve a fully dehydrated specimen.

#### Laser-induced self-healing of cuboid samples

The single-edge notch cuboid sample was fractured into two parts. The parts were assembled and placed into the original mold. A 1-mL (5  $\mu$ L enzyme, concentration: 2.9 mg/mL) of calcium enzyme solution was added to the crack region. Ultra-pure CO<sub>2</sub> was introduced on the surface for 15 min to precipitate the calcite crystals and form a prototype of the bridges. The sample was then settled for another 15 min, allowing the mineralization solution to penetrate naturally into the interior of the structure. The 3W laser was set up 2 cm above the sample and conducted on the crack for 6 h; then, the sample was able to be taken out of the mold.

#### Repairing procedure for ECM-n

ECM-n were fabricated and cured in a 3D print silicone mold with an elliptical and circular shape notch. After heating with the 3W laser for 12 h, the sample was taken out of the mold and transferred to a cubic silicon mold. The notch was filled with well-mixed sand-gelatin components, and the sample was then vibrated for 30 s A 200- $\mu L$  calcium-carbonic anhydrate mixed solution with nanoparticles was added on the notched surface and then aerated by  $CO_2$  for 15 min. This process should be slow enough to ensure that the solution penetrates to the bottom and does not affect the surrounding structures. A 3W laser was induced on the sample from the same distance on the repaired surface for 12 h and was finally taken out of the mold.

#### Mineralogical assessment of precipitates

The crystal and nanoparticles in ECM-n samples were segregated from the gelatin and sand matrix for assessment of the mineral phase in ECM-n after laser inducing for 12 h. Dried crystals and nanoparticle mixtures were ground with the mortar and smear mounted on a sample holder for fingerprint XRD. A Siemens D500 X-ray diffractometer analyzed the samples from to  $70^{\circ}$  20 using Cu K- $\alpha$  X-ray radiation with a step size of  $0.02^{\circ}$  and a dwell time of 2 s per step. Mineral phases were collected using a data collector. The laser-cured ECM-n was evaluated using JEOL JSM-7000F Analytical SEM Samples were first sputter coated with gold powder. EDS was used to assess the nanoparticle distribution in the ECM-n matrix.

#### Article



#### Raman spectroscopy

A hybrid system (XploRA, HORIBA, Montpellier, France) was used to obtain optical images and Raman spectra ranging from 100–1,200 cm $^{-1}$ . The experiment was used with a diode laser ( $\lambda$  = 785 nm), and the filter was set up at 10% and 100× objectives. The acquisition time and accumulation were defined as 5 and 20, respectively.

#### SUPPLEMENTAL INFORMATION

Supplemental information can be found online at https://doi.org/10.1016/j.xcrp. 2022.101039.

#### **ACKNOWLEDGMENTS**

The authors gratefully acknowledge the financial support from the National Science Foundation under award no. 2223664.

#### **AUTHOR CONTRIBUTIONS**

S.W., S.F.S., and N.R. designed the experiments. S.W. and N.R. analyzed the data and drafted the manuscript. S.W., S.F.S., and N.R. approved the final version of the manuscript.

#### **DECLARATION OF INTERESTS**

The authors declare no competing interests.

Received: July 11, 2022 Revised: August 9, 2022 Accepted: August 15, 2022 Published: September 2, 2022

#### **REFERENCES**

- Miller, S.A., and Moore, F.C. (2020). Climate and health damages from global concrete production. Nat. Clim. Chang 10, 439–443. https://doi.org/10.1038/s41558-020-0733-0.
- Ellis, L.D., Badel, A.F., and Chiang, M.L. (2020). Toward electrochemical synthesis of cement-An electrolyzer-based process for decarbonating CaCO3 while producing useful gas streams. Proc. Natl. Acad. Sci. USA 117, 12584–12591. https://doi.org/10.1073/pnas. 1821473116.
- 3. Hoenig, V., Hoppe, H., and Emberger, B. (2007). Carbon Capture Technology-Options and Potentials for the Cement Industry96 (European Cement Research Academy).
- Deja, J., Uliasz-Bochenczyk, A., and Mokrzycki, E. (2010). CO2 emissions from Polish cement industry. Int. J. Greenh. Gas Control 4, 583–588. https://doi.org/10.1016/j.ijggc.2010. 02.002.
- Wang, S., Scarlata, S.F., and Rahbar, N. (2022). A self-healing enzymatic construction material. Matter 5, 957–974. https://doi.org/10.1016/j. matt 2021 12 020
- Rilem, L.C. (1972). Functional classification of lightweight concretes. Mat. Constr. 5, 171–172. https://doi.org/10.1007/BF02539261.
- 7. Li, Y., Wen, K., Li, L., Huang, W., Bu, C., and Amini, F. (2020). Experimental investigation on

- compression resistance of bio-bricks. Constr. Build. Mater. 265, 120751. https://doi.org/10.1016/j.conbuildmat.2020.120751.
- Cheng, L., Kobayashi, T., and Shahin, M.A. (2020). Microbially induced calcite precipitation for production of "bio-bricks" treated at partial saturation condition. Constr. Build. Mater. 231, 117095. https://doi.org/10. 1016/j.conbuildmat.2019.117095.
- Haque, M.N., Al-Khaiat, H., and Kayali, O. (2004). Strength and durability of lightweight concrete. Cem. Con. Compos. 26, 307–314. https://doi. org/10.1016/S0958-9465(02)00141-5.
- Al-Khaiat, H., and Haque, M. (1998). Effect of initial curing on early strength and physical properties of a lightweight concrete. Cem. Concr. Res. 28, 859–866. https://doi.org/10. 1016/S0008-8846(98)00051-9.
- Li, Y., Wang, D., Ping, X., Zhang, Y., Zhang, T., Wang, L., Jin, L., Zhao, W., Guo, M., Shen, F., et al. (2022). Local hyperthermia therapy induces browning of white fat and treats obesity. Cell 185, 949–966. https://doi.org/10. 1016/j.cell.2022.02.004.
- O'Neal, D.P., Hirsch, L.R., Halas, N.J., Payne, J.D., and West, J.L. (2004). Photo-thermal tumor ablation in mice using near infraredabsorbing nanoparticles. Cancer Lett. 209,

- 171–176. https://doi.org/10.1016/j.canlet.2004.
- Varon, L.A.B., Orlande, H.R.B., and Eliçabe, G.E. (2016). Combined parameter and state estimation in the radio frequency hyperthermia treatment of cancer. Numer. Heat Tran. Part A Appl. 70, 581–594. https://doi.org/10.1080/ 10407782.2016.1193342.
- 14. Gas, P., and Miaskowski, A. (2015). Specifying the ferrofluid parameters important from the viewpoint of magnetic fluid hyperthermia. In 2015 Selected Problems of Electrical Engineering and Electronics (WZEE) (IEEE Xplore), p. 7394040.
- Kothandaraman, C.P. (2006). Fundamentals of Heat and Mass Transfer, Third edition (New Age International).
- Ramirez, S., Chan, K., Hernandez, R., Recinos, E., Hernandez, E., Salgado, R., Khitun, A., Garay, J., and Balandin, A. (2017). Thermal and magnetic properties of nanostructured densified ferrimagnetic composites with graphene - graphite fillers. Mater. Des. 118, 75–80. https://doi.org/10.1016/j.matdes.2017. 01.018.
- Diep, P., Pannem, S., Sweer, J., Lo, J., Snyder, M., Stueber, G., Zhao, Y., Tabassum, S., Istfan, R., Wu, J., et al. (2015). Three-dimensional printed optical phantoms with customized



## Cell Reports Physical Science Article

- absorption and scattering properties. Biomed. Opt. Express 6, 4212–4220. https://doi.org/10.1364/BOE.6.004212.
- 18. Kosky, P., Balmer, R., Keat, W., and Wise, G. (2020). Exploring Engineering Book, Fifth Edition (Academic Press).
- Van Wijk, W.R., and Scholte Ubing, D.W. (1963). Physics of Plant Environment (North-Holland Publishing Company), pp. 62–101. https://doi. org/10.1002/qj.49709038628.
- Kundakcioglu, E., Lazoglu, I., and Rawal, S. (2016). Transient thermal modeling of laser-based additive manufacturing for 3D freeform structures. Int. J. Adv. Manuf. Technol. 85, 493–501. https://doi.org/10.1007/s00170-015-7932-2
- Caiazzo, F., and Alfieri, V. (2018). Simulation of laser heating of aluminum and model validation via two-color pyrometer and shape assessment. Materials 11. https://doi.org/10. 3390/ma11091506.

- 22. Hammond, G., and Jones, C. (2011). Embodied Carbon. The Inventory of Carbon and Energy (ICE) (BSRIA).
- 23. Ashby, M. (2005). Materials Selection in Mechanical Design, Third edition (Elsevier Science & Technology Books).
- da Costa Ores, J., Sala, L., Cerveira, G.P., and Kalil, S.J. (2012). Purification of carbonic anhydrase from bovine erythrocytes and its application in the enzymic capture of carbon dioxide. Chemosphere 88, 255–259. https:// doi.org/10.1016/j.chemosphere.2012.03.059.
- Huijgen, W.J.J., and Comans, R.N.J. (2005). Carbon Dioxide Sequestration by Mineral Carbonation Literature Review. https://edepot. wur.nl/121870.
- Kumar, D., Chandra, M.V., Elavarasan, K., and Shamasundar, B.A. (2017). Structural properties of gelatin extracted from croaker fish (Johnius sp) skin waste. Int. J. Food Prop. 20, S2612–

- S2625. https://doi.org/10.1080/10942912.2017.1381702.
- Zurrer, T., Wong, K., Horlyck, J., Lovell, E.C., Wright, J., Bedford, N.M., Han, Z., Liang, K., Scott, J., and Amal, R. (2021). Mixed-metal MOF-74 templated catalysts for efficient carbon dioxide capture and methanation. Adv. Funct. Mater. 31, 2007624. https://doi.org/10. 1002/adfm.202007624.
- Zheng, Y., Zhang, W., Li, Y., Chen, J., Yu, B., Wang, J., Zhang, L., and Zhang, J. (2017). Energy related CO2 conversion and utilization: advanced materials/nanomaterials, reaction mechanisms and technologies. Nano Energy 40, 512–539. https://doi.org/10.1016/j.nanoen. 2017.08.049.
- Baltrusaitis, J., Schuttlefield, J., Zeitler, E., and Grassian, V.H. (2011). Carbon dioxide adsorption on oxide nanoparticle surfaces. Chem. Eng. J. 170, 471–481. https://doi.org/10. 1016/j.cej.2010.12.041.